Global Non-Hydrostatic Modeling Using Voronoi Meshes: The MPAS Model

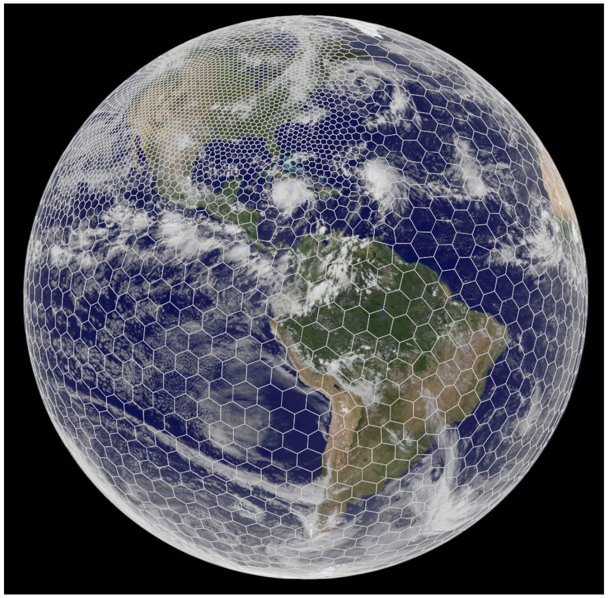

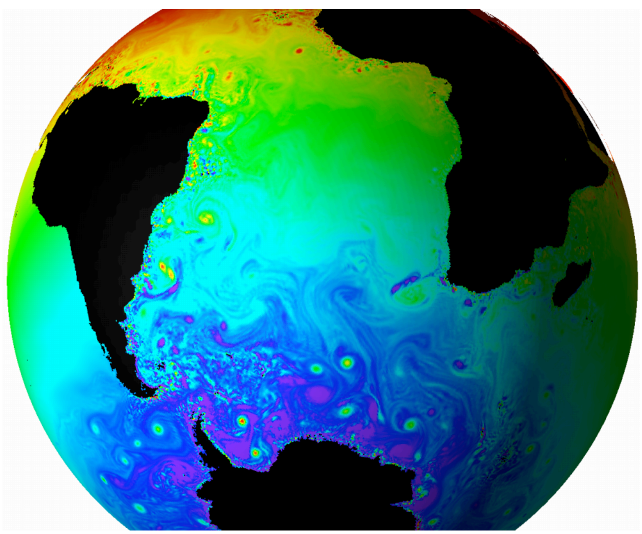

Model for Prediction Across Scales

Based on unstructured centroidal Voronoi (hexagonal) meshes using C-grid staggering and selective grid refinement.

Jointly developed, primarily by NCAR and LANL/DOE, for weather, regional climate, and climate applications

MPAS infrastructure - NCAR, LANL, others.

MPAS - Atmosphere (NCAR)

MPAS - Ocean (LANL)

MPAS - Ice, etc.

Bill Skamarock, Joe Klemp, Michael Duda,
Sang-Hun Park and Laura Fowler NCAR
Todd Ringler Los Alamos National Lab
John Thuburn Exeter University
Max Gunzburger Florida State University
Lili Ju University of South Carolina

Global Non-Hydrostatic Modeling Using Voronoi Meshes: The MPAS Model

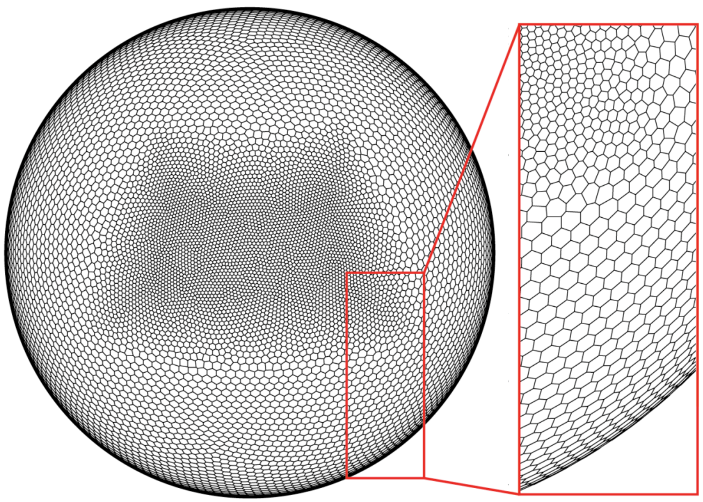

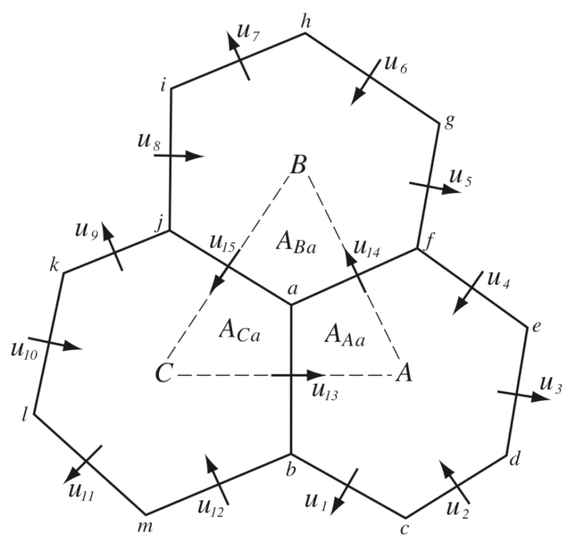

Applications
- NWP, Regional Climate, and Climate

Equations
- Fully compressible nonhydrostatic vector invariant form

C-grid centroidal Voronoi mesh
- Erroneous non-stationary geostrophic modes: our solution
- Accuracy and efficiency of transport schemes: higher accuracy second-order schemes

Test results

Global Non-Hydrostatic Modeling Using Voronoi Meshes: The MPAS Model

Variables:
$(U,V,\Omega,\Theta,Q_j) = \tilde{\rho}_d \cdot (u,v,\dot{\eta},\theta,q_j)$

Vertical coordinate:
$z = \zeta + A(\zeta)\,h_s(x,y,\zeta)$

Prognostic equations:

$$\frac{\partial \boldsymbol{V}_H}{\partial t} = -\frac{\rho_d}{\rho_m}\left[\boldsymbol{\nabla}_\zeta\left(\frac{p}{\zeta_z}\right) - \frac{\partial \boldsymbol{z}_H p}{\partial \zeta}\right] - \eta\,\boldsymbol{k}\times\boldsymbol{V}_H$$
$$-\boldsymbol{v}_H \boldsymbol{\nabla}_\zeta \cdot \boldsymbol{V} - \frac{\partial \Omega \boldsymbol{v}_H}{\partial \zeta} - \rho_d \boldsymbol{\nabla}_\zeta K - eW\cos\alpha_r - \frac{uW}{r_e} + \boldsymbol{F}_{V_H},$$

$$\frac{\partial W}{\partial t} = -\frac{\rho_d}{\rho_m}\left[\frac{\partial p}{\partial \zeta} + g\tilde{\rho}_m\right] - \left(\boldsymbol{\nabla}\cdot\boldsymbol{v}W\right)_\zeta$$
$$+\frac{uU+vV}{r_e} + e\left(U\cos\alpha_r - V\sin\alpha_r\right) + F_W,$$

$$\frac{\partial \Theta_m}{\partial t} = -\left(\boldsymbol{\nabla}\cdot\boldsymbol{V}\,\theta_m\right)_\zeta + F_{\Theta_m},$$

$$\frac{\partial \tilde{\rho}_d}{\partial t} = -\left(\boldsymbol{\nabla}\cdot\boldsymbol{V}\right)_\zeta,$$

$$\frac{\partial Q_j}{\partial t} = -\left(\boldsymbol{\nabla}\cdot\boldsymbol{V}\,q_j\right)_\zeta + \rho_d S_j + F_{Q_j},$$

Diagnostics and definitions:

$$\theta_m = \theta\left[1 + (R_v/R_d)q_v\right] \qquad p = p_0\left(\frac{R_d\zeta_z\Theta_m}{p_0}\right)^\gamma$$

$$\frac{\rho_m}{\rho_d} = 1 + q_v + q_c + q_r + \ldots$$

Equation set points of interest

- Prognostic equations for coupled variables.
- Generalized height coordinate.
- Horizontally vector invariant eqn set.
- Continuity equation for dry air mass.
- Thermodynamic equation for coupled potential temperature.

Integration scheme

As in Advanced Research WRF -
Split-explicit Runge-Kutta (3rd order)

Hexagonal C-Grid Problem:
Non-Stationary Geostrophic Mode

Traditional Coriolis velocity evaluation

$$\partial_t u_1 + g\delta_{x_1} h + \frac{f}{\sqrt{3}}(u_{31} - u_{21}) = 0$$

$$\partial_t u_2 + g\delta_{x_2} h + \frac{f}{\sqrt{3}}(u_{12} - u_{32}) = 0$$

$$\partial_t u_3 + g\delta_{x_3} h + \frac{f}{\sqrt{3}}(u_{23} - u_{13}) = 0$$

$$\partial_t h + \tfrac{2}{3}H(\delta_{x_1} u_1 + \delta_{x_2} u_2 + \delta_{x_3} u_3) = 0$$

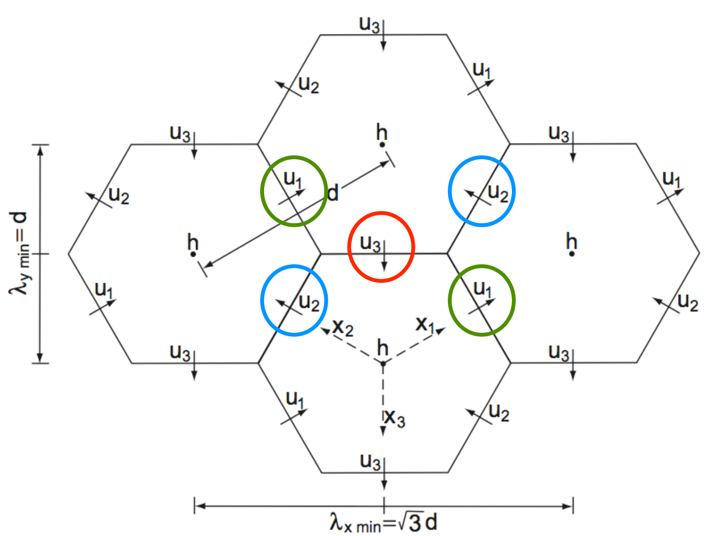

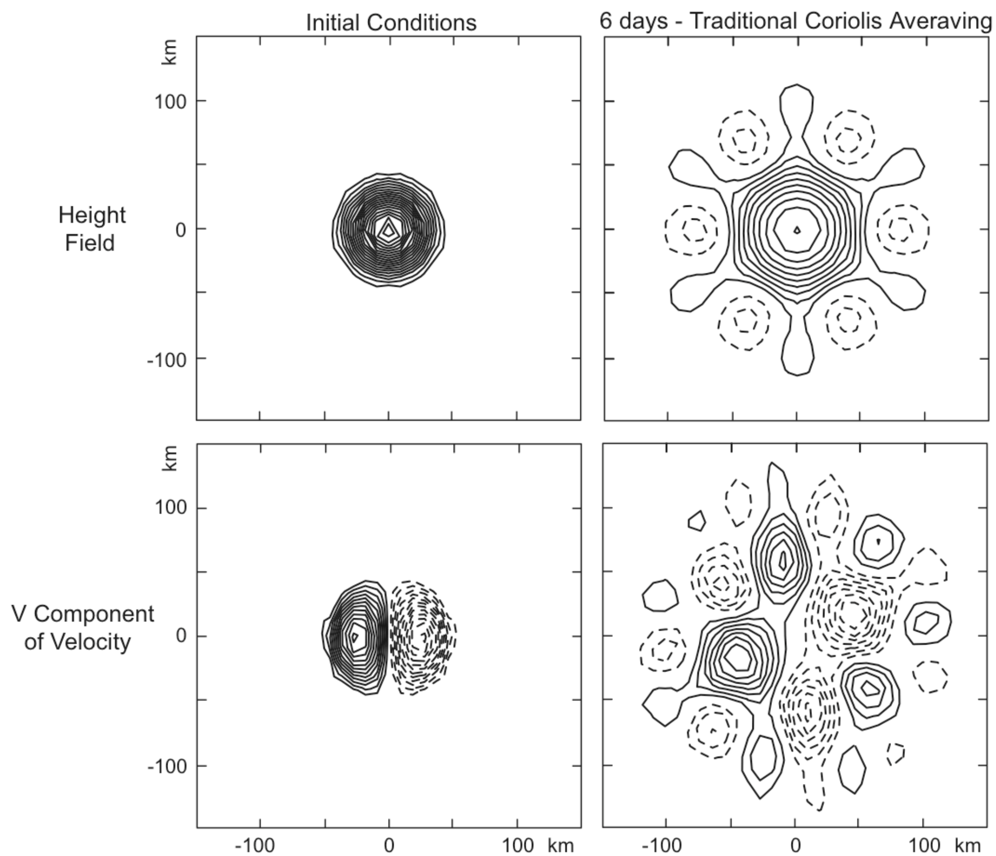

(see Nickovic et al MWR 2002)

Hexagonal C-Grid Problem: Non-Stationary Geostrophic Mode

New Coriolis velocity evaluation (Thuburn, 2008 JCP)

$$\partial_t u_1 + g\delta_{x_1} h + \frac{f}{\sqrt{3}}(u_{31} - u_{21}) = 0$$

$$\partial_t u_2 + g\delta_{x_2} h + \frac{f}{\sqrt{3}}(u_{12} - u_{32}) = 0$$

$$\partial_t u_3 + g\delta_{x_3} h + \frac{f}{\sqrt{3}}(u_{23} - u_{13}) = 0$$

$$\partial_t h + \tfrac{2}{3}H(\delta_{x_1} u_1 + \delta_{x_2} u_2 + \delta_{x_3} u_3) = 0$$

$$u_{21} = \tfrac{1}{3}\overline{u_2}^{x_3} + \tfrac{2}{3}\overline{\overline{u_2}^{x_1}}^{x_2}, \quad u_{31} = \tfrac{1}{3}\overline{u_3}^{x_2} + \tfrac{2}{3}\overline{\overline{u_3}^{x_1}}^{x_3},$$

$$u_{12} = \tfrac{1}{3}\overline{u_1}^{x_3} + \tfrac{2}{3}\overline{\overline{u_1}^{x_1}}^{x_2}, \quad u_{32} = \tfrac{1}{3}\overline{u_3}^{x_1} + \tfrac{2}{3}\overline{\overline{u_3}^{x_2}}^{x_3},$$

$$u_{13} = \tfrac{1}{3}\overline{u_1}^{x_2} + \tfrac{2}{3}\overline{\overline{u_1}^{x_1}}^{x_3}, \quad u_{23} = \tfrac{1}{3}\overline{u_2}^{x_1} + \tfrac{2}{3}\overline{\overline{u_2}^{x_2}}^{x_3}$$

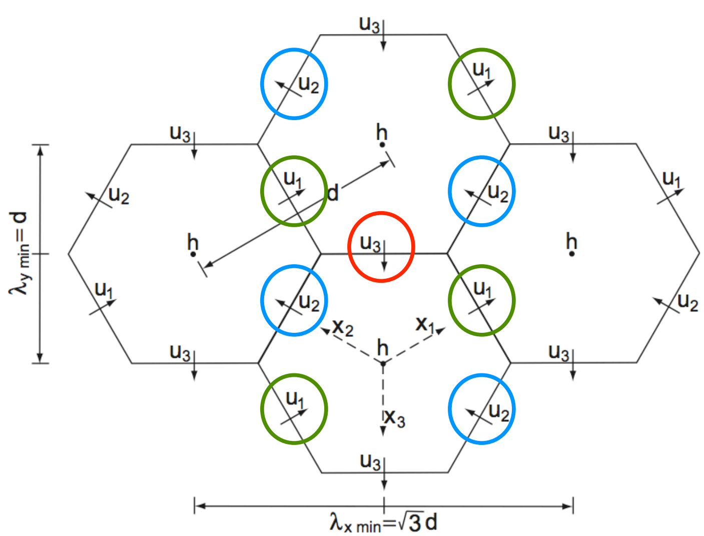

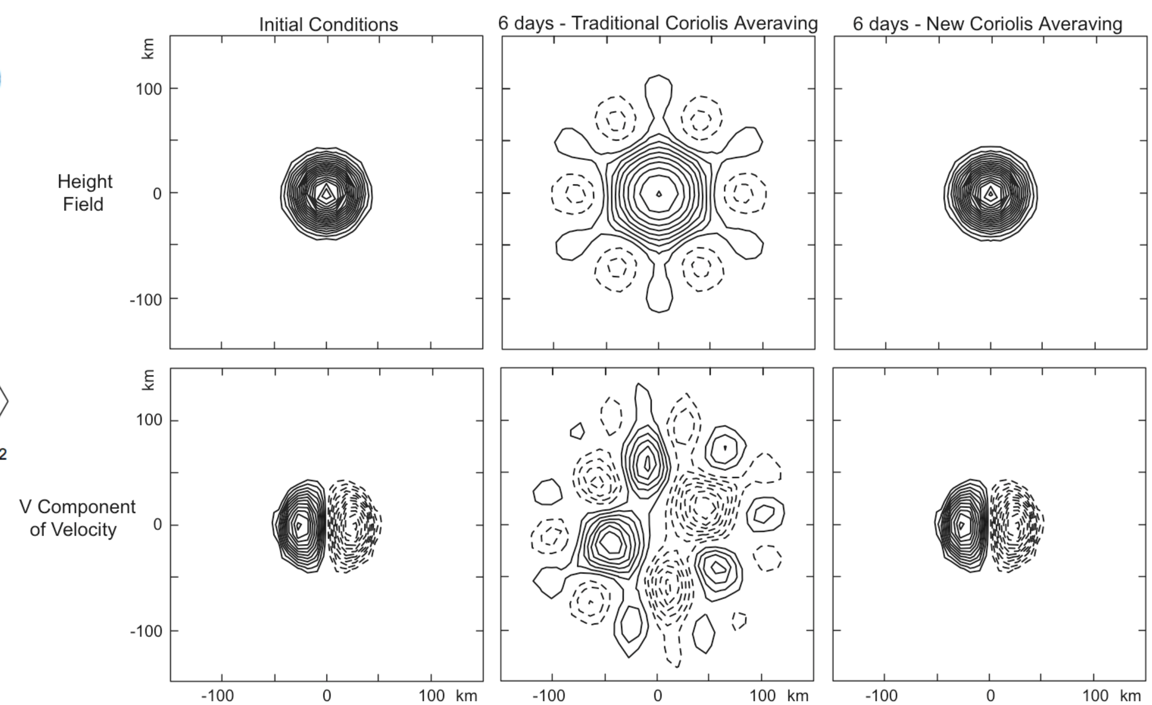

Thuburn (2008) Tangential Velocity Reconstruction

In the discrete analogue of vorticity equation (ξ_τ=-fδ_a), the divergence δ_a on the Delaunay triangulation is identical to the divergence δ_A on the Voronoi hexagons used in the height equation (h_t=-Hδ_A) integrated over the triangle.

$$A_a\delta_a = \frac{A_A\delta_A + A_B\delta_B + A_C\delta_C}{6}$$

Divergence δ_A in hexagon A:

$$A_A\delta_A = \sum_{i=1}^{6} l_i u_i \cdot \mathbf{n}_i$$

Divergence δ_a in triangle ABC:

$$A_a\xi_t = -f A_a\delta_a = f\sum_{j=1}^{3} d_j u_j^{\perp} \cdot \mathbf{n}_j$$

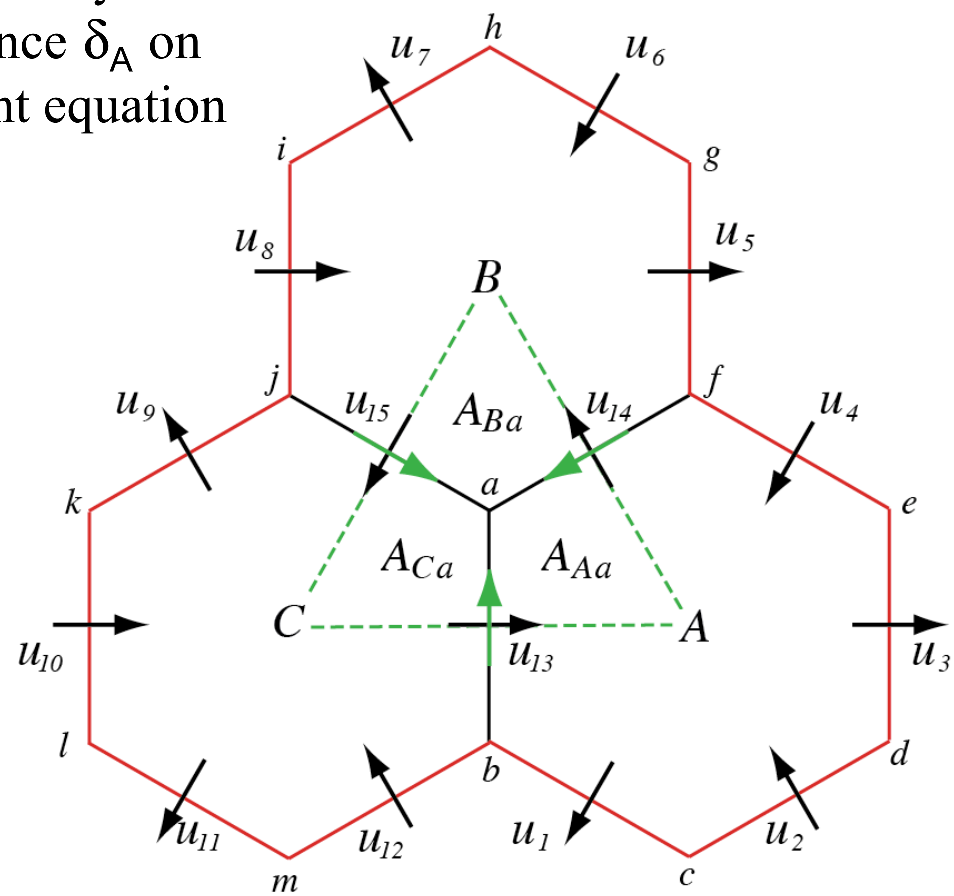

Generalization for Irregular Hexagons

Construct tangential velocities from weighted sum of (10) normal velocities on edges of adjacent hexagons.

Careful choice of additional constraints leads to a solution for the weights w_e^j that depend only on the triangle/polygon area ratios local to the shared polygon.

The general tangential velocity reconstruction produces a consistent divergence on the primal and dual grids, and allows for PV, enstrophy and energy* conservation in the nonlinear SW solver.

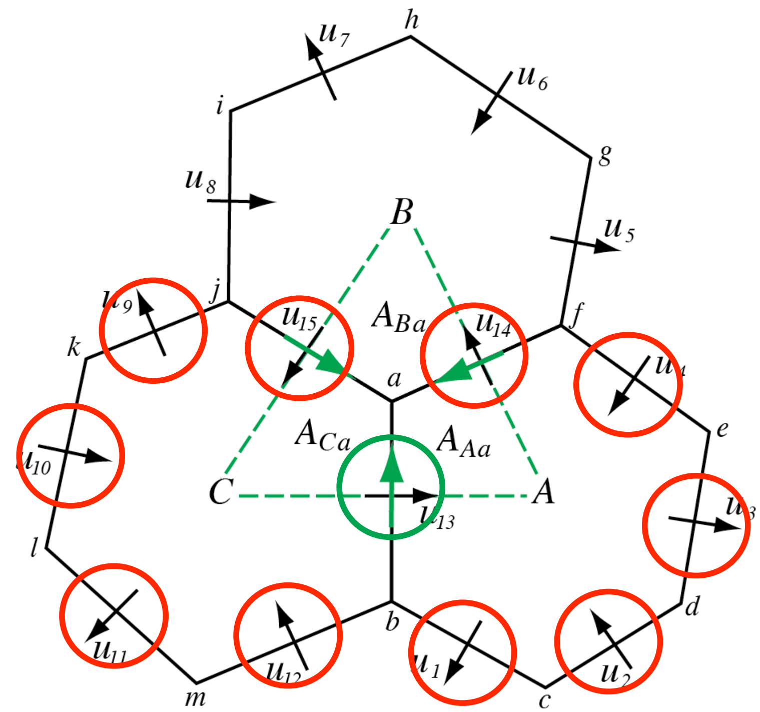

Generalization for Irregular Hexagons

Our tangential velocity reconstruction is valid for any Voronoi grid
(3, 4, 5, 6, 7… *n* sided cells)

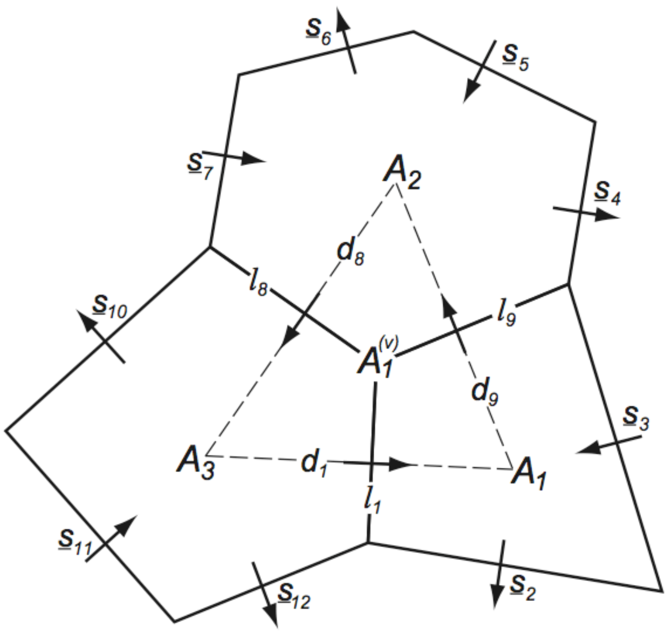

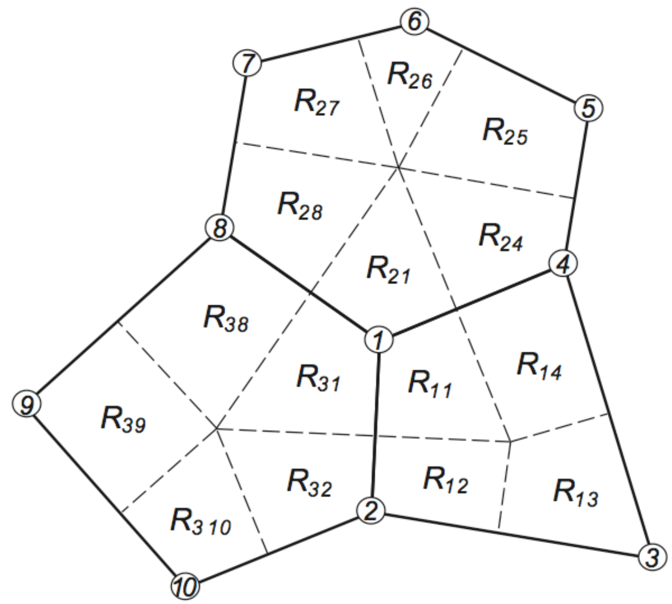

General formulation should be regarded as an extension of
Sadourny (JAS, 1975) and Arakawa and Lamb (MWR, 1981)

Runge-Kutta Based Transport

MPAS uses a Runge-Kutta time-integration scheme.

$$\frac{\partial(\rho\psi)}{\partial t} = L(\mathbf{V}, \rho, \psi)$$

$$(\rho\psi)^{*} = (\rho\psi)^{t} + \frac{\Delta t}{3} L(\mathbf{V}, \rho, \psi^{t})$$

$$(\rho\psi)^{**} = (\rho\psi)^{t} + \frac{\Delta t}{2} L(\mathbf{V}, \rho, \psi^{*})$$

$$(\rho\psi)^{t+\Delta t} = (\rho\psi)^{t} + \Delta t\, L(\mathbf{V}, \rho, \psi^{**})$$

$$(\rho\psi)_i^{t+\Delta t} = (\rho\psi)_i^{t} - \Delta t \frac{1}{A_i} \sum_{n_{e_i}} d_{e_i} (\rho \mathbf{V} \cdot \mathbf{n}_{e_i}) \psi$$

Instantaneous
flux divergence in
RK-based scheme

Computing the flux - consider 1D transport (e.g. from WRF)

$$\frac{\partial(u\psi_i)}{\partial x} = \frac{1}{\Delta x}\left[F_{i+1/2}(u\psi) - F_{i-1/2}(u\psi)\right] + O(\Delta x^p).$$

2nd-order flux: $F(u,\psi)_{i+1/2} = u_{i+1/2}\left[\frac{1}{2}(\psi_{i+1} + \psi_i)\right]$

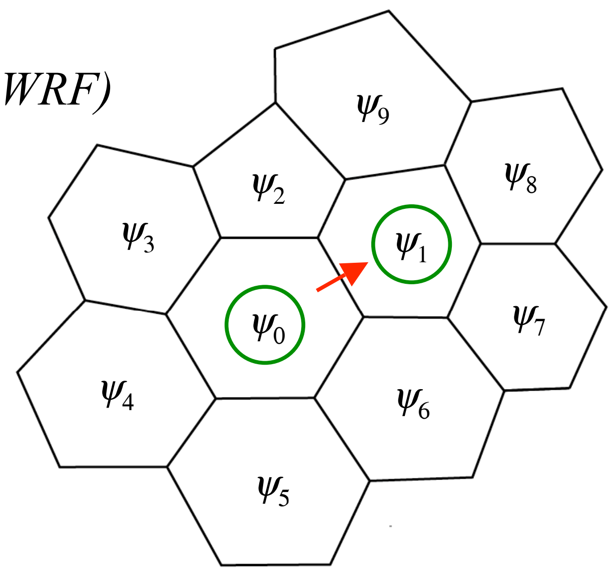

Runge-Kutta Based Transport

3rd and 4th-order fluxes:

$$F(u,\psi)_{i+1/2} = u_{i+1/2}\left[\frac{1}{2}\left(\psi_{i+1}+\psi_i\right) - \frac{1}{12}\left(\delta_x^2\psi_{i+1}+\delta_x^2\psi_i\right) + sign(u)\,\frac{\beta}{12}\left(\delta_x^2\psi_{i+1}-\delta_x^2\psi_i\right)\right]$$

where $\delta_x^2\psi_i = \psi_{i-1} - 2\psi_i + \psi_{i+1}$ *(Hundsdorfer et al, 1995; Van Leer, 1985)*

Recognizing $\delta_x^2\psi = \Delta x^2 \dfrac{\partial^2\psi}{\partial x^2} + O(\Delta x^4)$ recast the 3rd and 4th order flux as

$$F(u,\psi)_{i+1/2} = u_{i+1/2}\left[\frac{1}{2}\left(\psi_{i+1}+\psi_i\right) - \Delta x_e^2\frac{1}{12}\left\{\left(\frac{\partial^2\psi}{\partial x^2}\right)_{i+1} + \left(\frac{\partial^2\psi}{\partial x^2}\right)_i\right\}\right.$$
$$\left. + \,sign(u)\,\Delta x_e^2\frac{\beta}{12}\left\{\left(\frac{\partial^2\psi}{\partial x^2}\right)_{i+1} - \left(\frac{\partial^2\psi}{\partial x^2}\right)_i\right\}\right]$$

where x is the direction normal to the cell edge and i and $i+1$ are cell centers. We use the least-squares-fit polynomial to compute the second derivatives.

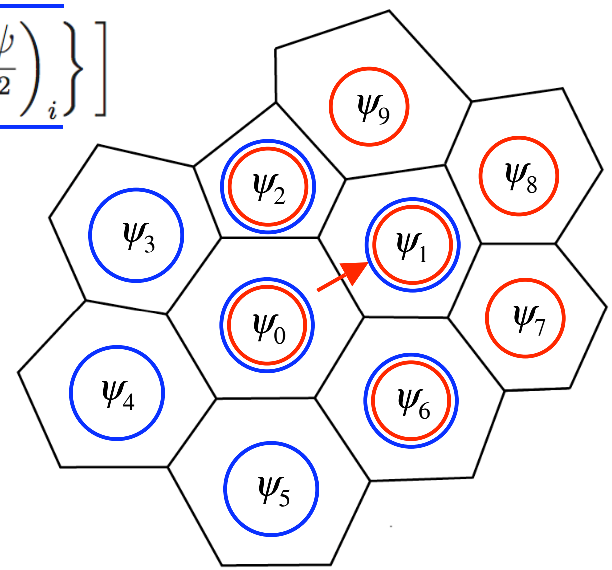

Runge-Kutta Based Transport

Extension to Voronoi (hexagonal) meshes

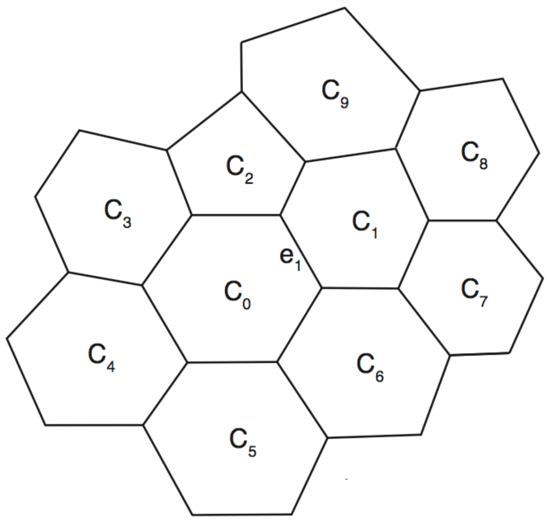

Edge e_1 has weights for computing second derivatives at cell centers C_0 and C_1.

The weights for C_0 apply to cell centers C_0 through C_6, and the weights for C_1 apply to cell centers C_0-C_2 and C_6-C_9.

$$(\rho\psi)^* = (\rho\psi)^t - \frac{\Delta t}{3}\frac{1}{A_i}\sum_{n_{e_i}} d_{e_i}(\rho\mathbf{V})^t \cdot n_{e_i}\,\psi^t$$

$$(\rho\psi)^{**} = (\rho\psi)^t - \frac{\Delta t}{2}\frac{1}{A_i}\sum_{n_{e_i}} d_{e_i}(\rho\mathbf{V})^* \cdot n_{e_i}\,\psi^*$$

$$(\rho\psi)^{t+\Delta t} = (\rho\psi)^t - \Delta t\,\frac{1}{A_i}\sum_{n_{e_i}} d_{e_i}(\rho\mathbf{V})^{**} \cdot n_{e_i}\,\psi^{**}$$

Monotonic or PD limiter is applied on the final RK substep if desired.

Runge-Kutta Based Transport

Deformational Flow Test Case

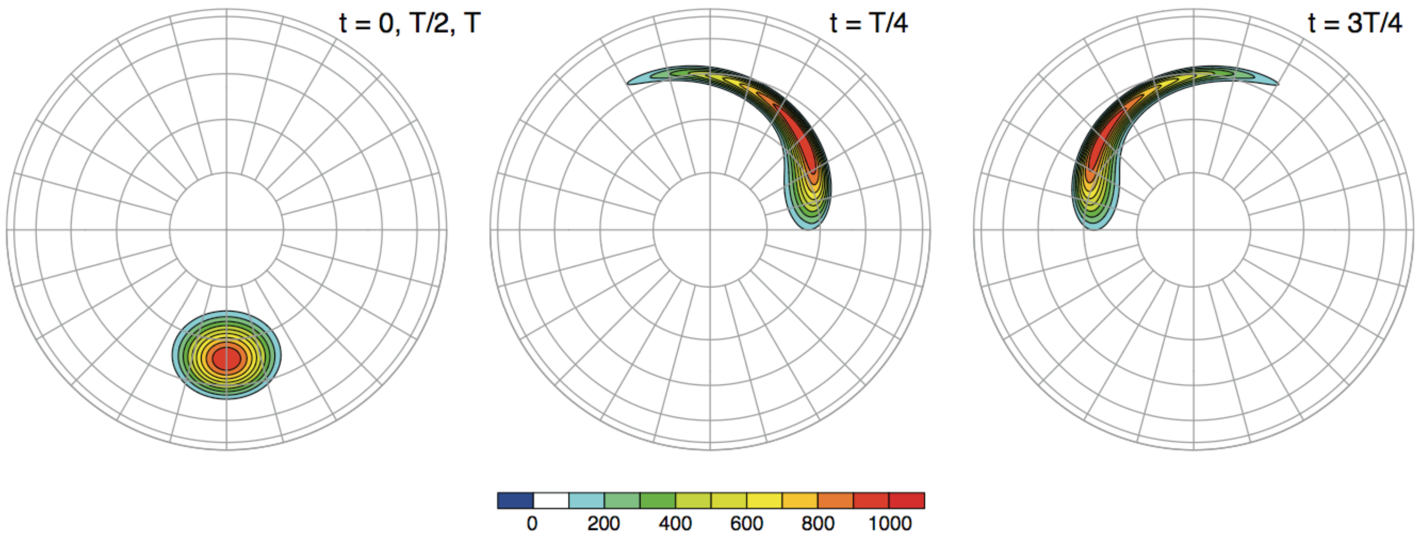

FIG. 8. Blossey and Durran (2008) test problem mapped to the sphere.

Runge-Kutta Based Transport

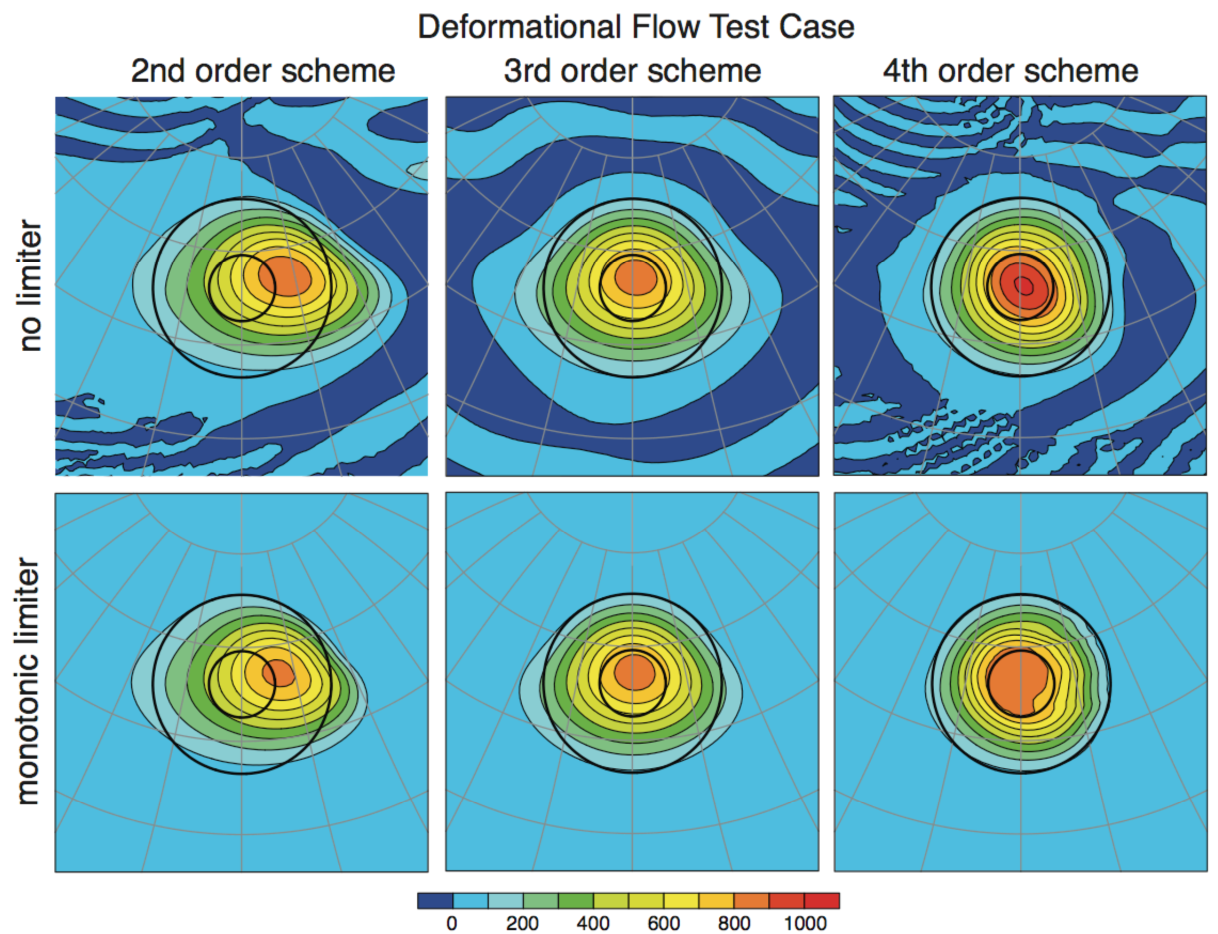

FIG. 5. Deformational flow test case results at time T. The thick contours are the exact solution for $\psi = 100$ and 800. The simulations were performed on the 40962-cell grid.

Runge-Kutta Based Transport

$$F(u,\psi)_{i+1/2} = u_{i+1/2}\left[\frac{1}{2}(\psi_{i+1}+\psi_i) - \Delta x_e^2 \frac{1}{12}\left\{\left(\frac{\partial^2\psi}{\partial x^2}\right)_{i+1} + \left(\frac{\partial^2\psi}{\partial x^2}\right)_i\right\}\right.$$
$$\left. + \, sign(u)\,\Delta x_e^2 \frac{\beta}{12}\left\{\left(\frac{\partial^2\psi}{\partial x^2}\right)_{i+1} - \left(\frac{\partial^2\psi}{\partial x^2}\right)_i\right\}\right]$$

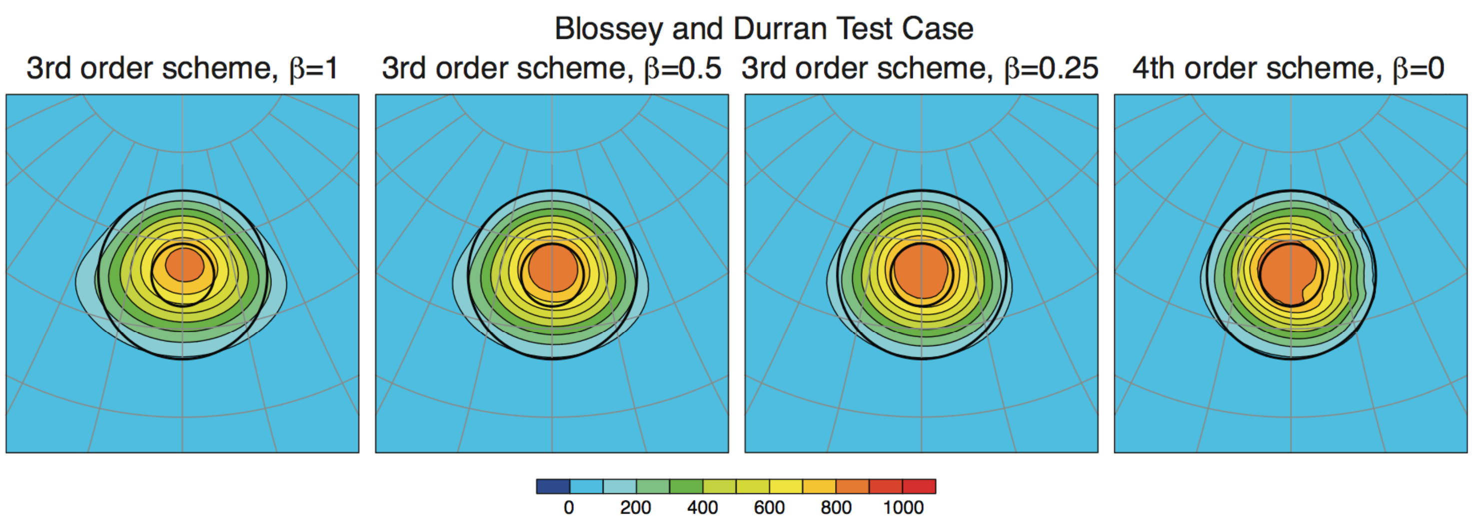

FIG. 7. Deformational flow test case results at time T using (11) with different values of the filter parameter β. The simulations were performed on the 40962-cell grid.

Runge-Kutta Based Transport

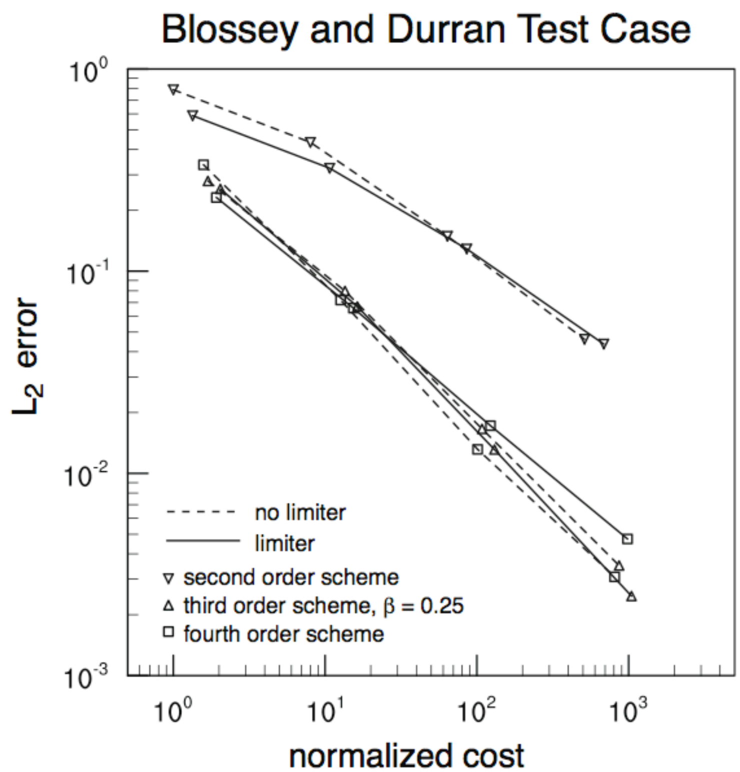

MPAS nonhydrostatic core

Jablonowski and Williamson (2006) baroclinic wave test case, day 9

~120 km cell spacing

$\Delta t = 900$ s
$\Delta\tau = 150$ s
26 levels

Vertically-stretched grid.

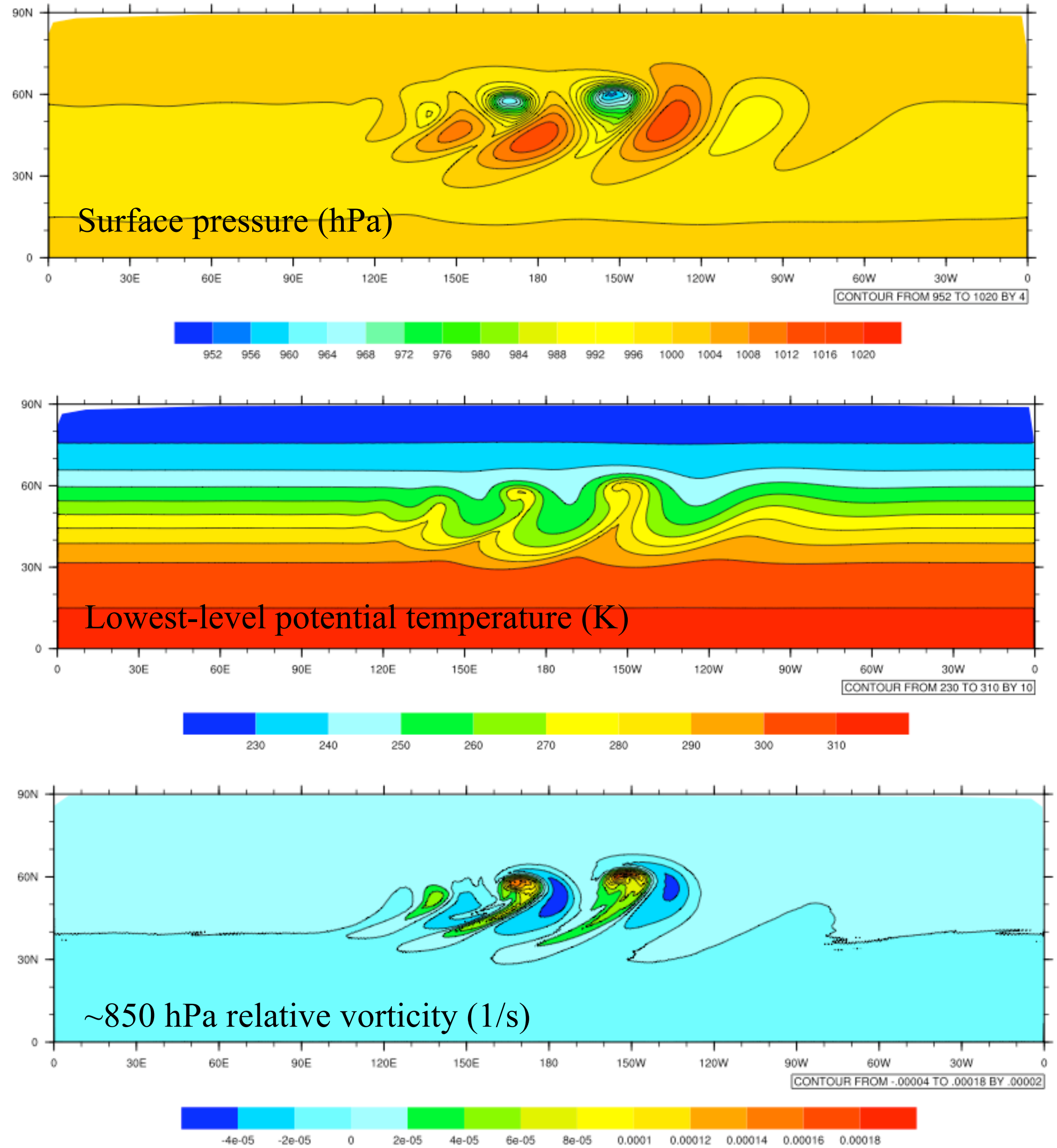

Jablonowski and Williamson (2006) Baroclinic Wave Test
Phase Errors for the GME and Nonhydrostatic MPAS Models

(errors computed from 655362 cell reference solution, ~ 30 km dx)

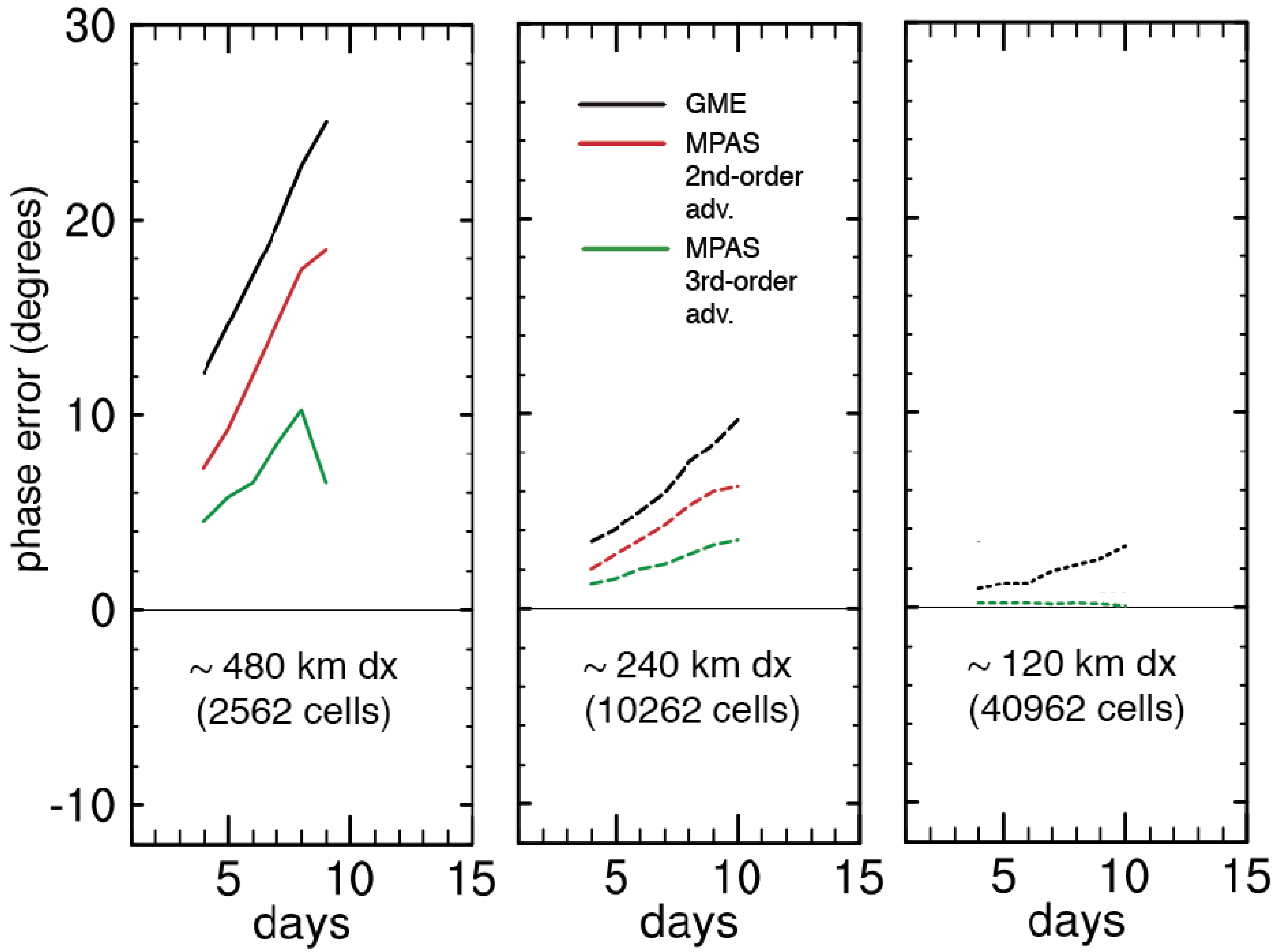

GME results from Jablonowski and WIlliamson (2006) QJ vol. 132 (621), figure 12.

MPAS nonhydrostatic core

Global variable-resolution moist baroclinic waves

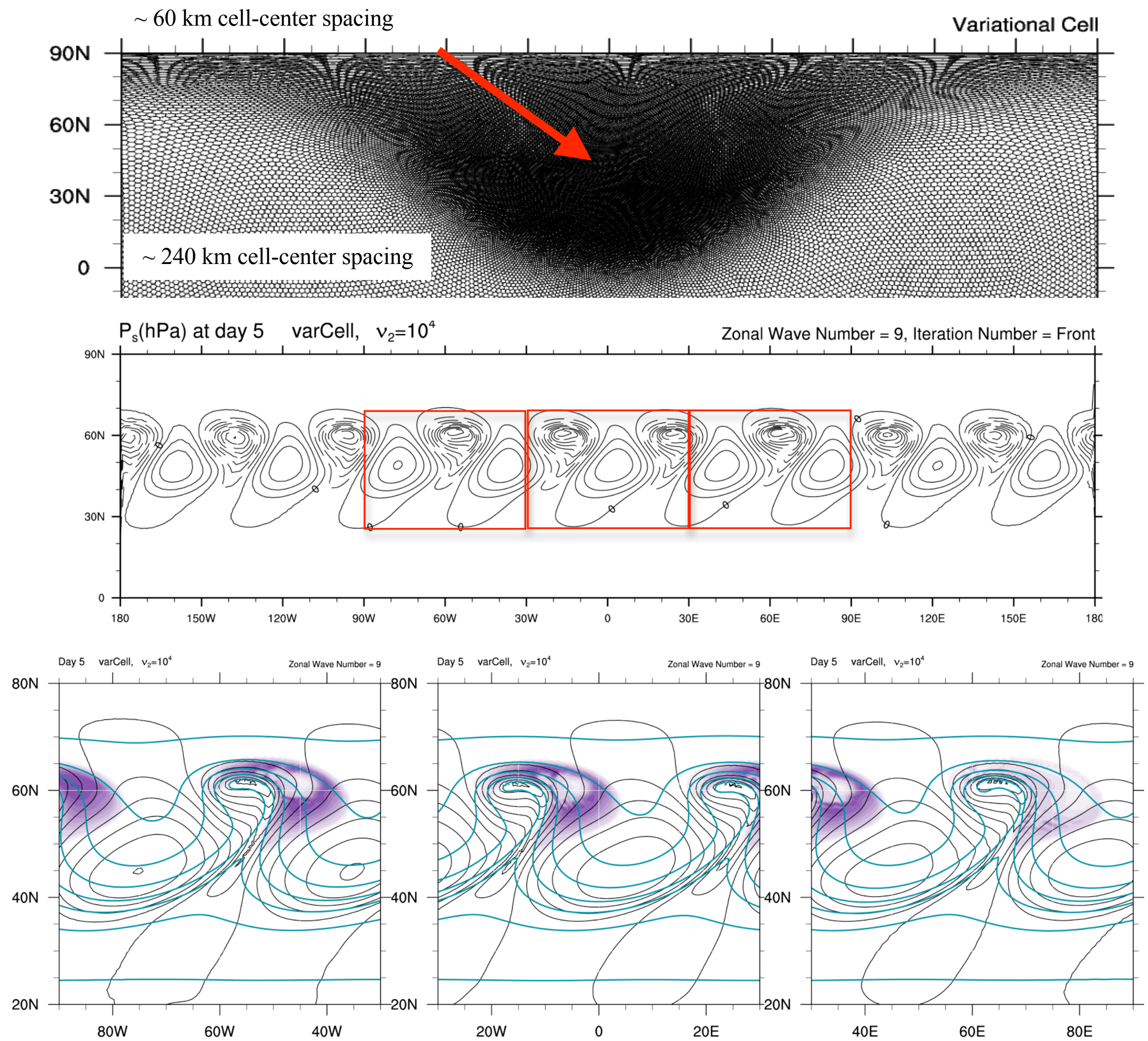

MPAS nonhydrostatic core

2D (y,z) simulations
Based on 3D doubly
periodic (*x*,*y*) config.

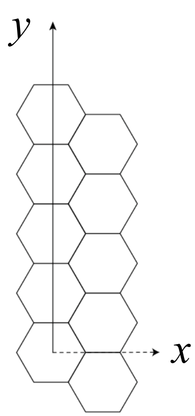

Straka et al (1993)
density current simulations

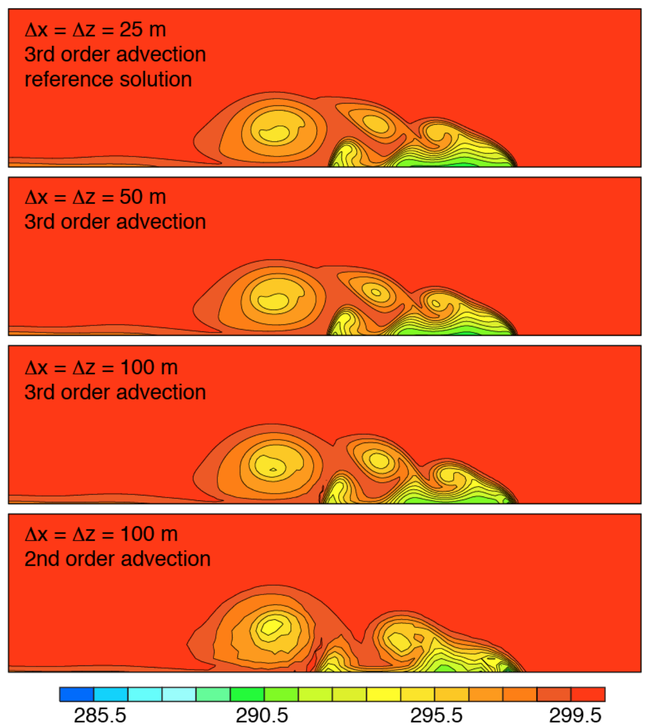

Schar test case

Vertical velocity c.i. = 0.05 m/s

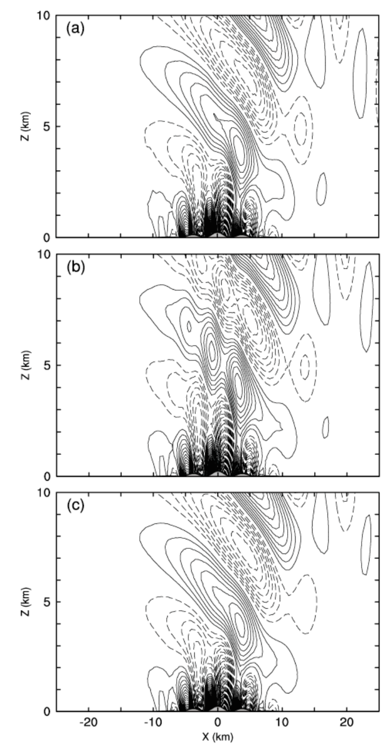

Θ 2nd order
Ω 2nd order

Θ 4th order
Ω 2nd order

Θ 4th order
Ω 4th order

$$\frac{\partial \Theta_m}{\partial t} = -\boldsymbol{\nabla} \cdot \boldsymbol{V}\, \theta_m + F_{\Theta_m}$$

$$\begin{aligned}\Omega_i &= \boldsymbol{V} \cdot \boldsymbol{\nabla} \zeta = \zeta_z \boldsymbol{V} \cdot \boldsymbol{\nabla}(z - z_i) \\ &= \zeta_z \left[\boldsymbol{\nabla} \cdot \boldsymbol{V}(z - z_i) - (z - z_i)\boldsymbol{\nabla} \cdot \boldsymbol{V}\right] \\ &= \zeta_z \boldsymbol{\nabla} \cdot \boldsymbol{V}(z - z_i)\end{aligned}$$

Squall-Line Tests

Low-level shear (0-2.5 km), Weisman-Klemp sounding
Warm-bubble perturbation, results at 3 hours

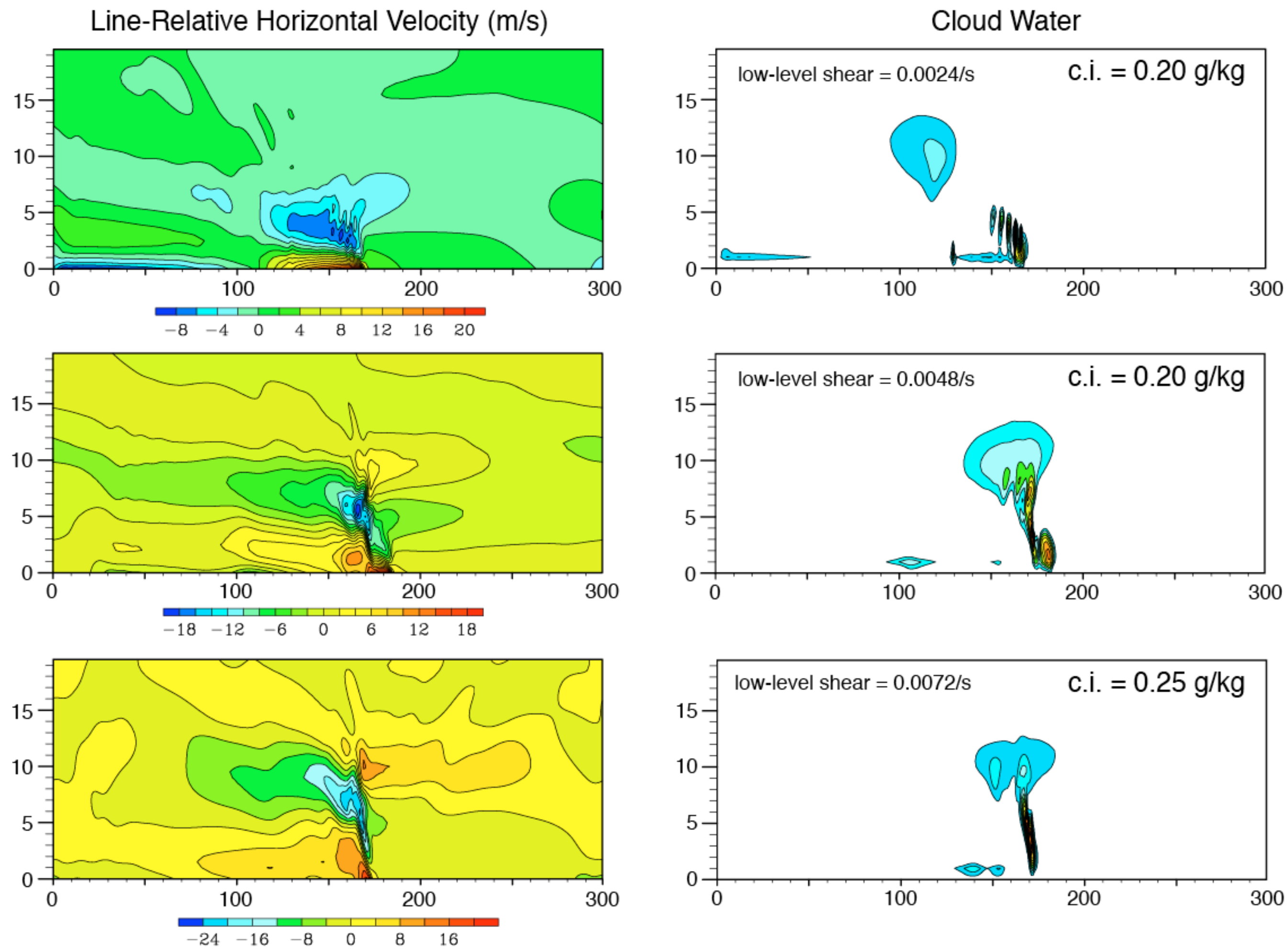

(from Max Menchaca)

Supercell Tests

Low-level shear (0-5 km, 30 m/s), Weisman-Klemp sounding,
Warm-bubble perturbation, Periodic in x and y (Lx, Ly ~ 84 km),
3D (x,y,z) simulations, Δh = 500 m

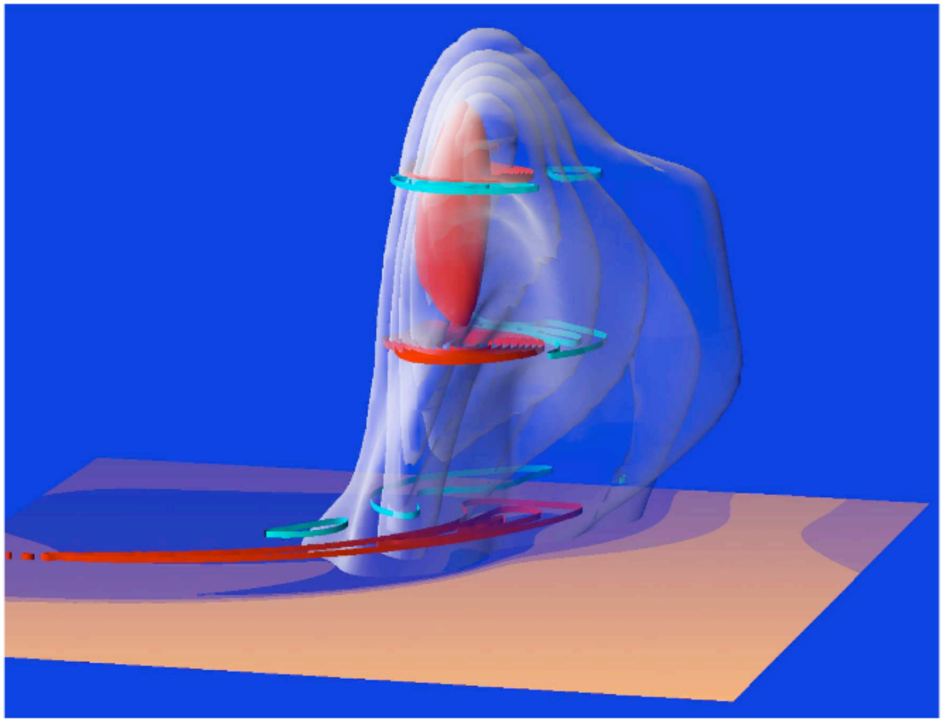

(a) Hexagonal mesh simulation

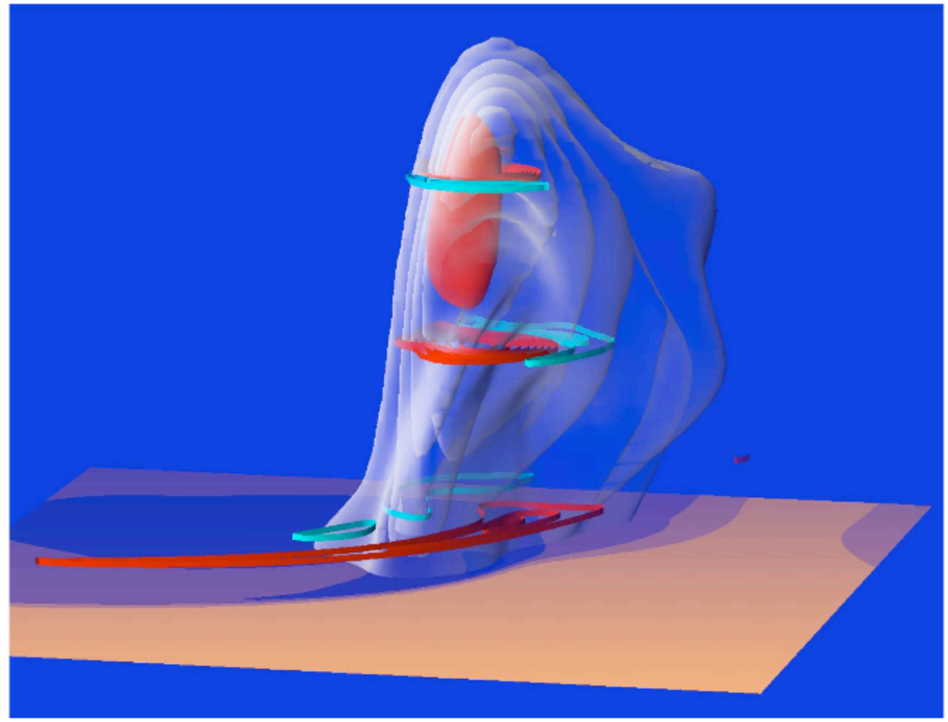

(b) Rectangular mesh simulation

Vertical velocity contours at 1, 5, and 10 km (c.i. = 3 m/s)

30 m/s vertical velocity surface shaded in red

Rainwater surfaces shaded as transparent shells

Perturbation surface temperature shaded on baseplane

MPAS - Summary

SW solver for SVCT unstructured C-grid

- Recovers stationary geostrophic mode.
- SW solver conserves PV, energy to time truncation.
- Solutions comparable to existing SW solvers, and no dissipation needed for standard SW test cases.

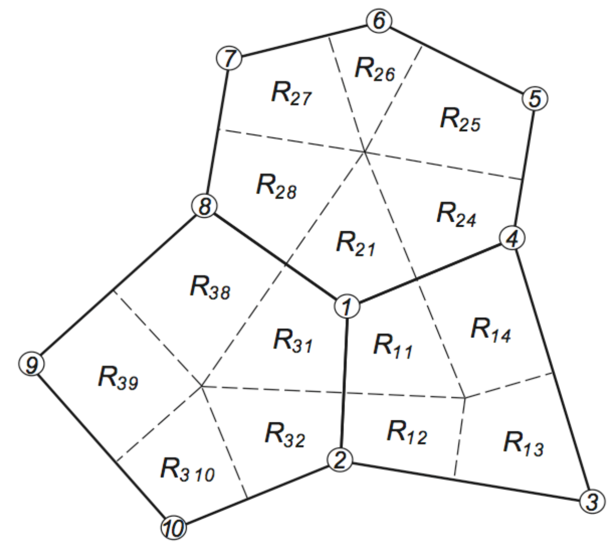

3D Solvers

- Hydrostatic 3D SVCT solver (based on SW solver - parallel).
- Variable-resolution grid results are encouraging.
- Nonhydrostatic 3D SVCT solver (based on hydrodstatic solver).
- Both solvers work on the sphere and 2D and 3D Cartesian domains.
- Moist tests results confirm viability of Voronoi C-grid discretization.

Test Suites

- Moist baroclinic-wave tests allow us to quickly access robustness of our solvers on the sphere, accelerate development.
- Ability to use nonhydrostatic solver in 2 and 3D Cartesian-domain tests allows direct comparison with existing established solvers.

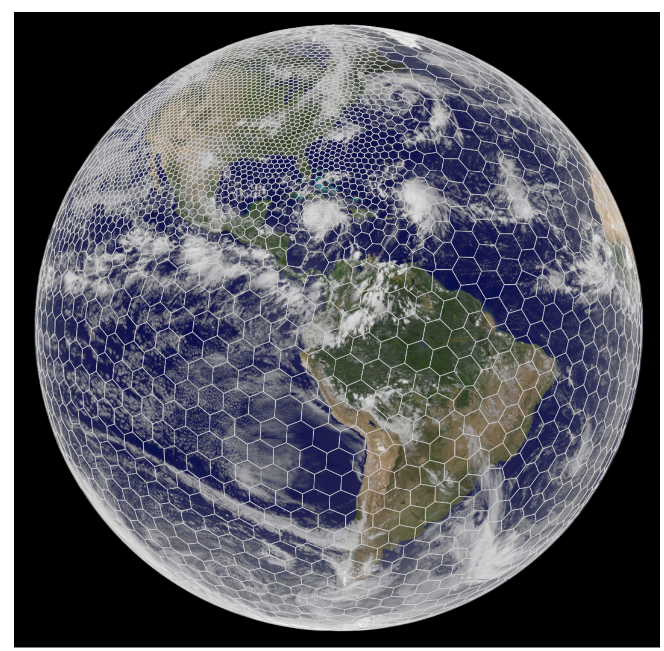

Future Development

- Weather, regional climate and climate physics suites.
- Further testing of variable resolution meshes, physics development.
- Further development and testing of higher-order transport schemes.